Contents lists available at ScienceDirect

Journal of Materials Research and Technology

Microstructural engineering in carbon steel walls printed by directed energy deposition to enhance mechanical properties through heat-input control

Yasamin Khebreh Farshchi [a], Farzad Khodabakhshi [a], Maryam Mohri [b,*], Hassan Shirazi [a], Mahmoud Nili-Ahmadabadi [a,**]

[a] School of Metallurgy and Materials Engineering, College of Engineering, University of Tehran, Tehran, Iran
[b] EMPA, Swiss Federal Laboratories for Materials Science and Technology, Dübendorf, 8600, Switzerland

ARTICLE INFO

ABSTRACT

The main object of the present study is focused on the systematic processing heat-input design based on directed energy deposition (DED) methodology, enrolling carbon steel phase transformation to control the mechanical properties. Three different 4-layer low-carbon alloy steel (ER70S-6) walls are fabricated to investigate this matter with varying heat-inputs. To justify heat-inputs, single layers by metal-inert gas (MIG) welding with different heat-inputs were carried out, and the results were used as input data to the 4-layers fabrication. In addition, to get a more homogenous structure, some walls' heat-inputs have descended from the first layer to the top layer. The microstructural studies show that reducing heat-input causes a higher solidification rate and the formation of finer columnar grains, which significantly affects the mechanical properties. Electron microscopy analysis reveals that a higher cooling rate in the wall with descending heat-input from bottom to top (496 J/mm to 382 J/mm), motivates formation of the acicular ferrite and bainite, which significantly enhances the mechanical properties. The exceptional tensile toughness of the wall, ~28.86 GPa%, with an ultimate tensile strength (UTS) of ~740 MPa, yield stress of ~560 MPa, and an elongation to failure of ~38 % depicted the impact of fine and multi-constituents' microstructure by heat-input control.

1. Introduction

Over the past few years, there has been a growing interest in additive manufacturing (AM) owing to its ability to produce parts at high speeds and its economic advantages in manufacturing. Furthermore, AM employed for the fatigue strengthening of damaged metallic members [1,2]. Compared to traditional methods like machining and forging, AM technologies provide several advantages [3], including developing complex or specialized features straight from the designed part without using expensive tooling or forms, less material wastage, and a significant level of product accuracy [4].

Wire Arc Additive Manufacturing (WAAM) is one of the sub-categories of Directed Energy Deposition (DED) AM technology. WAAM as a promising alternative for the production of large-scale metallic parts with relatively low to medium structural complexity, use welding to manufacture the designed part [5]. In this method, the wire and a part of the substrate are melted by an electric arc from the power source, allowing the material to be deposited on top of the substrate layer by layer to create the desired preform. Additionally, shielding gas is used to protect the melt pool throughout the process [6]. The controlling parameters of this process are voltage, current, and speed of movement for the construction of the final piece [7]. These parameters determine the heat-input that affects the size of the molten pool.

The AM-specific grain structures formed during the complex thermal cycle and rapid cooling rates associated with various AM methods to achieve a more homogeneous structure [8]. Recent studies in mini-mizing microstructural inhomogeneity in parts fabricated via WAAM used post-process heat treatment. For example, the post-process heat treatment, including solutionizing and aging, significantly improved the microstructural inhomogeneity of the maraging steel part fabricated by WAAM method [9]. The tensile properties of thin-walled parts of the die

---

* Corresponding author.
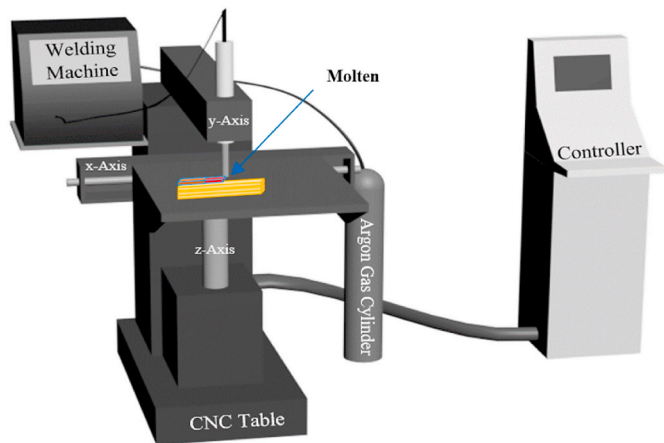** Corresponding author.

Fig. 1. The scheme of the WAAM processing set-up.

steel H13 exhibited anisotropy, but annealing for 4 h at 830 °C could potentially make them isotropic. However, the annealing process resulted in a reduction in hardness, tensile strength, and yield strength [10].

ER70S steel is known for its excellent weldability due to its low carbon content and high levels of silicon and manganese. It produces high-quality welds with good penetration, and minimal spatter [11]. Bellamkonda et al. [12] successfully produced an ER70S-6 steel cylindrical component. The microstructure of this part varied between the lower and upper regions, culminating in a range of ultimate tensile strength (UTS) from 429 MPa to 589 MPa, respectively. Therefore, in order to achieve more homogeneous properties, post-fabrication treatment was required. Nemani et al. [13] investigated the impacts of inter-critical austenitizing temperature on the microstructure and mechanical properties of ER70S-6 part fabricated by WAAM process. The water-quenched WAAM specimen formed an ideal microstructure leading to a great combination of ductility and strength in the printed part and eliminating the anisotropic flexibility. After that, they studied the effect of post-printing heat treatments cycles, including hardening and normalizing heat treatment. Although the hardening heat treatment increased the tensile strength, it intensified the ductility anisotropy of horizontal and vertical samples, but the anisotropy in mechanical

properties and homogeneity of the microstructure were minimized by normalizing as a heat treatment due to the removal of the coarse grain areas in the HAZ [14].

The anisotropy and heterogeneity in the mechanical properties of metallic AM parts are mostly related to the as printed microstructure, including; crystallographic texture, grain morphology, phase transformation, lack-of-fusion defects, microstructural coarsening, and heterogeneous recrystallization layer banding [15]. The heat-input also impacts the development of residual stress, internal defects, distortion, and affects the microstructure heterogeneity [16]. As a result, adjusting the heat-input significantly affects the microstructure and mechanical properties of the printed part.

The multi heat-input technique and using a lower heat-input in top layers from the substrate (by reducing the welding current or increasing the travel speed) leads to improved lamination dimensions in comparison to a fixed heat-input laminate wall [17]. The mixed heat-input (MHI) strategy aimed at minimizing voids and collapse defects that frequently occur during the fabrication of large block components while maintaining high manufacturing efficiency. By applying different heat-input conditions at various positions of the layer, it is possible to manufacture components that are free of defects, possess a uniform shape, and have no voids. This approach surpasses the conventional WAAM process [18]. Recent studies have explored post-printing heat treatment as a means of achieving homogeneity in mechanical properties. However, there has been limited research on obtaining uniform mechanical properties through the control of heat-input across different layers.

This study investigates the effect of adaptive heat-input control (means variation of heat-input versus wall/layer) on the microstructure

Table 2
Welding parameters used for each specimen are shown in Fig. 3.

Sample	Arc voltage (v)	Intensity (A)	Power (W)	Welding speed (mm/min)	Heat-input (J/mm)
A	11.6	103	1195	150	382
B	11.9	112	1333	150	426
C	12.1	120	1452	150	465
D	12.3	126	1550	150	496
E	12.4	132	1637	150	523
F	12.5	138	1725	150	552

Table 1
Nominal chemical compositions (in *wt*%) of the wire and substrate used in this work.

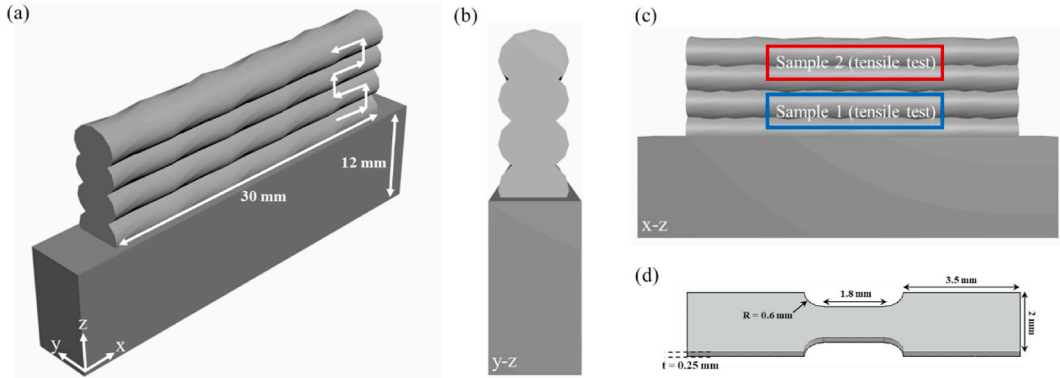|		C	Mn	Si	P	S	Ni	Cr	Mo	Fe
Wire	ER70S-6	0.072	1.248	0.761	0.015	0.0053	0.008	0.014	0.002	Bal.
Substrate	ST-37	0.15	0.491	0.073	0.008	0.009	0.03	0.001	0.008	Bal.

Fig. 2. Schematic of (a) the 4-layered wall produced by WAAM and deposition strategy, (b) the cross-section used for the metallographic sample, (c) tensile test standard coupon, and (d) sample 1 and 2 locations for tensile testing.
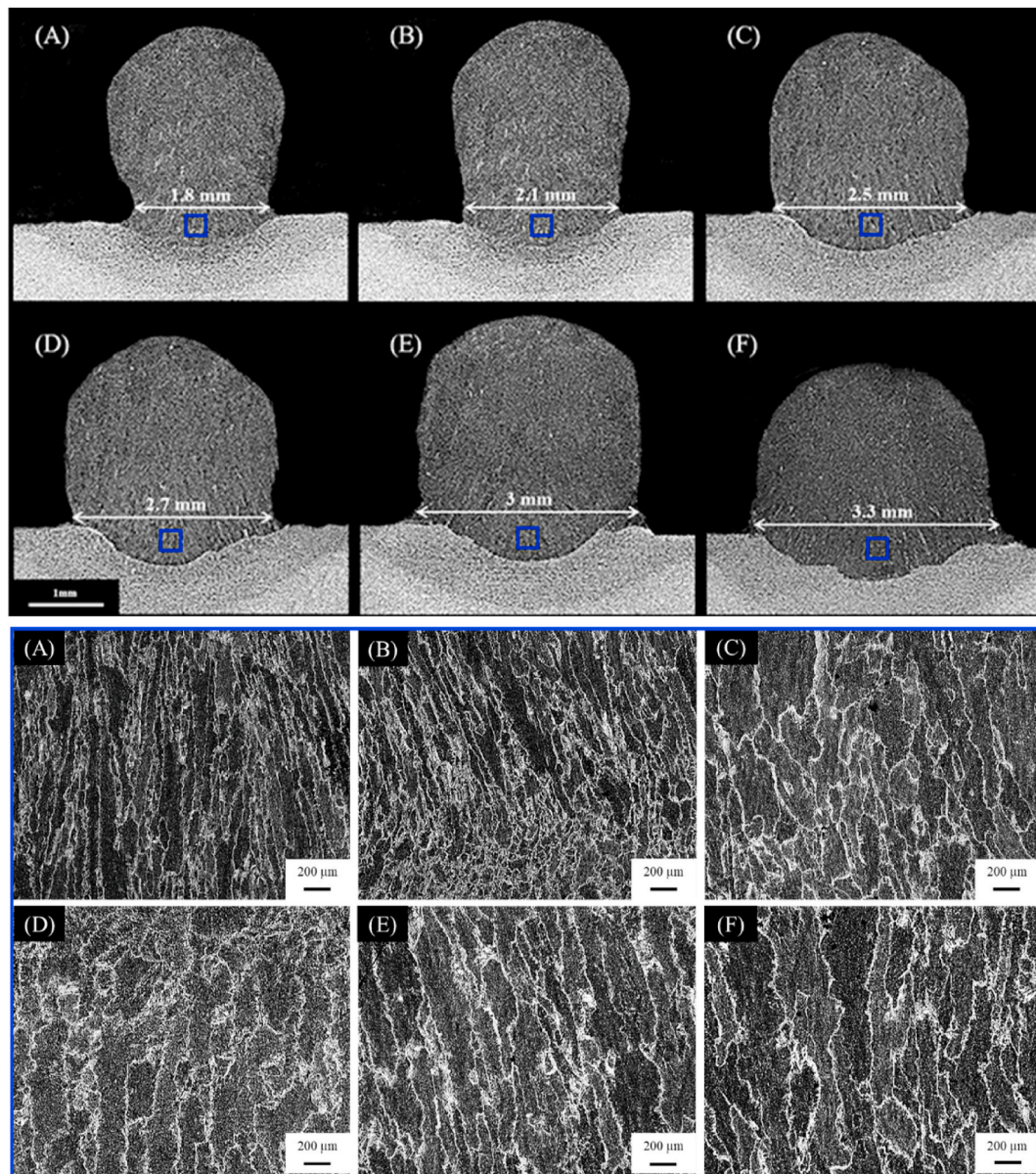
Fig. 3. One layer of MIG welding with corresponding microstructure undergoing various heat-inputs: (A) 382 J/mm; (B) 426 J/mm; (C) 465 J/mm; (D) 496 J/mm; (E) 523 J/mm; (F) 552 J/mm.

and mechanical properties of low-carbon alloy steel (ER70S-6) parts fabricated by WAAM based on gas metal arc welding (GMAW) technology. Special attention was paid to controlling and engineering the microstructural homogeneity of the wall by implying descending layer's heat-input. ST-37 steel, which has a very similar chemical composition to the counterpart alloy used as a reference and is the same as the substrate material. As the leading object, the correlation between the designed microstructure enrolling the possible phase transformations with the functional performance of the deposited walls in terms of indentation hardness and tensile properties was considered.

2. Materials and methods

2.1. Material and fabrication process

A three-axis CNC table combined with a GMAW welding machine was used to manufacture parts undergoing a typical WAAM methodology. Steel wire was fed into the welding machine, and the designed piece was constructed layer-by-layer with the aid of a CAD model. A schematic

illustration of the employed machine is shown in Fig. 1. The substrate was set up on the table and secured with clamps. The controller ran the G-code file, the table moved in response to the controller's commands, and the piece was produced following the designed plan.

An ER70S steel wire with a diameter of 0.8 mm was conducted in this study. Six single-layer MIG welding samples with a length of 30 mm and power (arc voltage × intensity) range of 1725 to 1195 W with a constant welding speed of 150 mm/min were constructed on the ST-37 substrate with a thickness of 12 mm to investigate the effect of heat-input. Then, according to the results of the former experiment, three four-layer walls with a length of 30 mm with different input power and constant welding speed of 150 mm/min were constructed to investigate the effect of heat-input on the WAAM process. The following strategies are used to print the walls: the first wall with layer-by-layer reduced power from a range of 1725 W–1452 W (wall 1), the second wall with a constant input power of 1452 W (wall 2), and the third wall with layer by layer reduced power from range 1550 W–1195 W (wall 3). The composition of the wire and substrate is shown in Table 1.

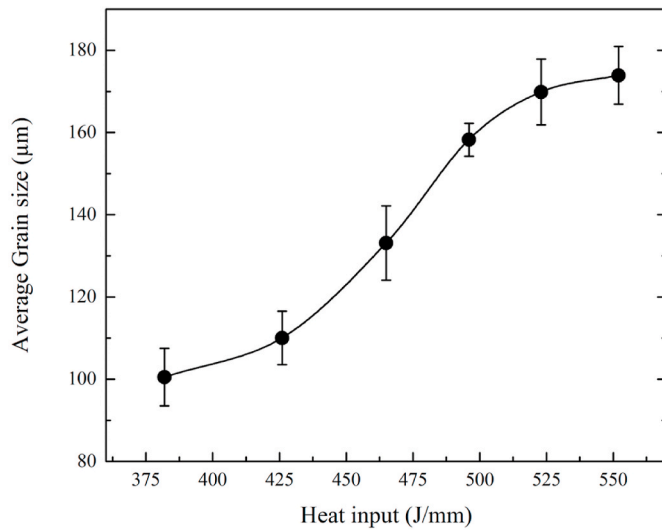An A2R CNC controller performed the deposition process with the

Fig. 4. The columnar grain size varies based on the heat-input curve.

CAD model pathway and a DIGI-MIG 210 welding machine with a pure Argon shielding gas flow rate of 8 L/min. A schematic of the walls manufactured using the WAAM method is shown in Fig. 2a. The deposition strategy is shown with arrows.

2.2. Microstructural characterization

A Schematic of the 4-layered wall produced by WAAM and deposition strategy is illustrated in Fig. 2a. Fig. 2b shows a schematic of metallographic samples extracted by conventional machining of the inner surface of additive manufactured walls. Microstructural characterizations were carried out using optical microscopy (OM) and scanning electron microscopy (SEM). For the OM and SEM observations, the samples were ground through 60, 400, 800, 1200, and 2000 grit SiC papers, followed by alumina (the size of ~1 μm) polishing. The polished samples were etched with a solution of Nital (5 % nitric acid and 95 %

ethanol) to reveal the grain structure. The grain size of each layer was measured based on the standard intercept method (ASTM E112).

To well understanding the phase transformation behavior of wall 3, the thermal history of the wall was adopted by using an Adamel DT1000 dilatometer. cylindrical sample with 10 mm in length and 2 mm in diameter were cut from the wall and placed in an infrared heating furnace under a vacuum of about 0.1 Pa. The samples were heated to 950 °C with a heating rate of 90 °C/s and isothermally held for 15 min followed by quenching with a cooling rate of 80 °C/s to 490 °C and held for 40 min at this temperature.

2.3. Mechanical properties evaluation

Hardness values were measured at 0.3 mm intervals of the columnar grain area of each layer using a 100 g force load and a 10-s dwell time. The highest and lowest values of seven distinct points were removed, and the resulting average hardness values were reported.

For the tensile tests, the walls were sliced in the vertical direction (x-z) with standard thickness, and after slicing, each wall was converted into 2 slices, and sample 1 and sample 2 were separated lengthwise to perform the tensile test. Fig. 2c is actually a schematic of a slice cut from the printed wall and shows the position of samples 1 and 2 for tensile testing. Miniature specimens with a gauge length of 1.8 mm and a cross-section area of 0.8 mm × 0.2 mm with uniform width(w) to thickness(t) ratio (w/t) of 4 were prepared due to the limited dimensions of the samples [19,20]. The uniform elongation, YS, and UTS values presented by Kumar et al. [20] nearly stabilized at 0.25 mm for thickness(t) and 1 mm for uniform width(w) (w/t = 4). Tensile testing was carried out in compliance with ASTM E8M − 16 employing a testing machine, the STM-20 Santam. The results of the tensile tests were reported as the average of at least three measurements with the appropriate standard deviation. Tensile tests were conducted at room temperature using a Santam universal testing machine with an initial cross-head speed of 0.01 mm/min [16]. A schematic of the tensile testing sample is presented in Fig. 2d.
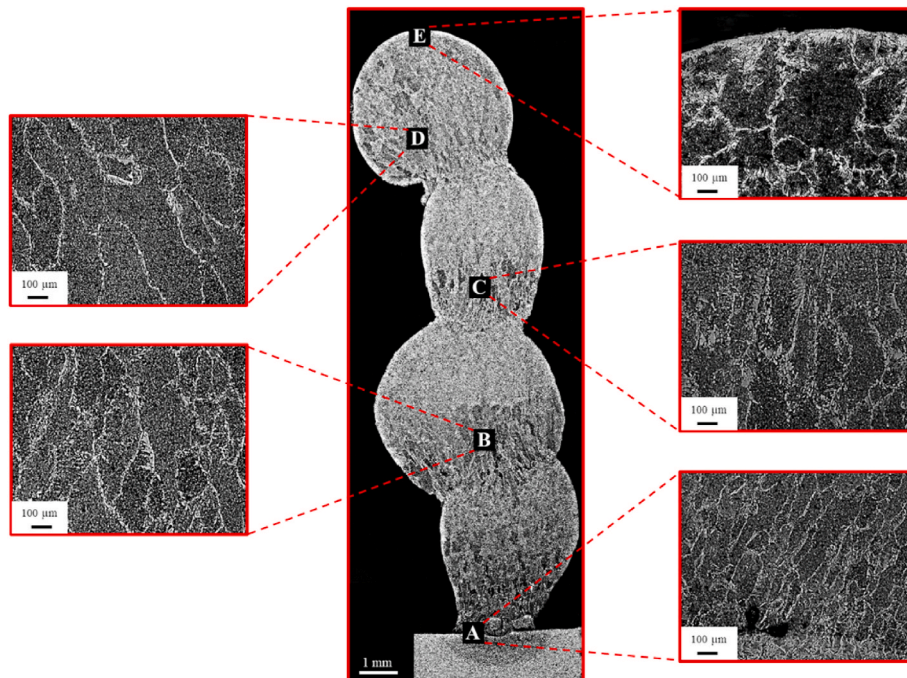

Fig. 5. Wall No.1 with heat-inputs of 552 J/mm for A, 523 J/mm for B, 496 J/mm for C, and 465 J/mm for D, and E is the equiaxed grains of the top layer.
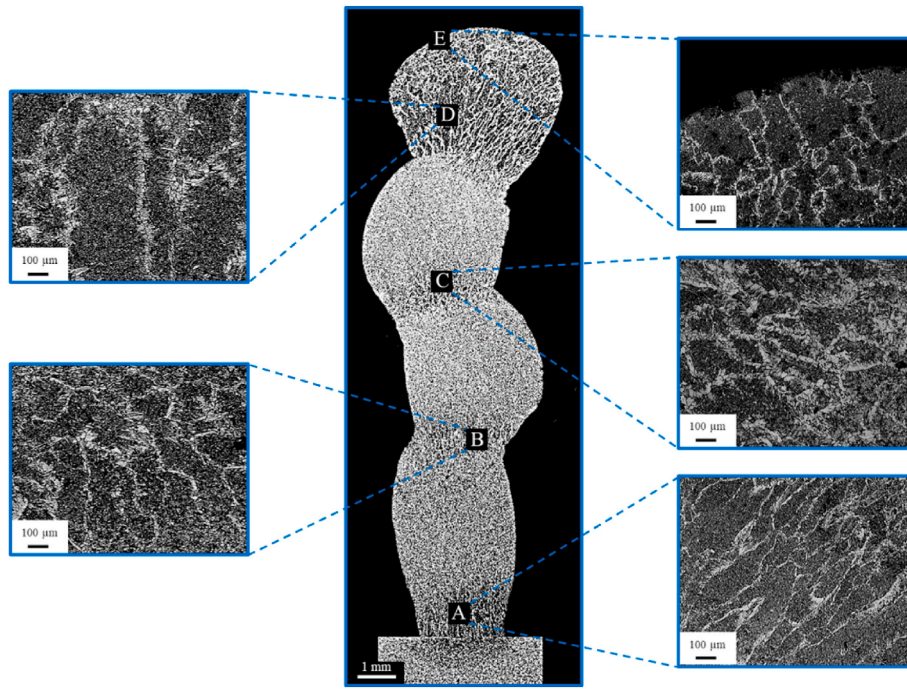
Fig. 6. Wall No.2 with heat-inputs of 465 J/mm for A, B, C, and D, and E is the equiaxed grains of the top layer.
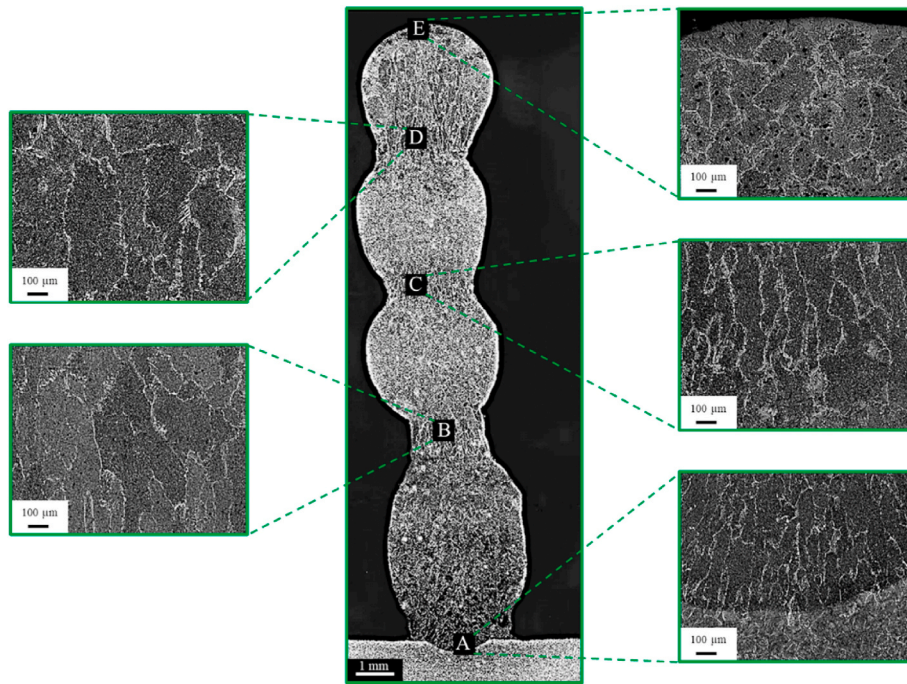

Fig. 7. Wall No.3 with heat-inputs of 496 J/mm for A, 465 J/mm for B, 426 J/mm for C, and 382 J/mm for D, and E is the equiaxed grains of the top layer.

3. Results and discussion

3.1. The effects of heat-input on the microstructure of as-built walls

In the welding process, the input parameters significantly affect the macro and microstructure properties along with the mechanical properties. Three crucial factors (voltage, current, and welding speed) directly influence the amount of heat-input during the welding process [21]. Heat-input has a direct relationship with current, voltage, and thermal efficiency value, as well as has an inverse relationship with the

welding speed [22]. Heat-input is usually calculated based on the following equation (1):

$$HI = \mu \frac{V.I}{S} \tag{1}$$

where *HI* is the heat-input (in J/mm), *V* is the arc voltage (in volts), *I* is the arc current (in Amperes), *S* is the welding speed (in mm/s), and μ is the thermal efficiency (until-less), which could typically be considered with a constant value of ~0.8 in MIG processing [23].

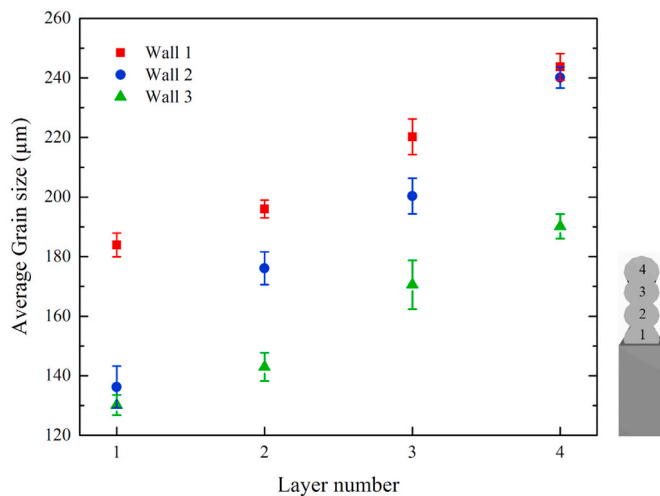Since heat-input influences the microstructure and for tailor making

Fig. 8. The columnar grain size per layer curves in walls manufactured by the WAAM process.

the process, first, six single-layer samples (A-F) with different heat-inputs, as listed in Table 2, were fabricated. Following, their microstructures were studied. The microstructure results of samples with different heat-input are shown in Fig. 3; the higher heat-input causes weld widening, which is due to the higher volume of the molten pool and melting of the substrate. Due to the temperature gradient between the molten metal and the substrate, the primary heat sink is oriented to the substrate, leading to columnar grains that are oriented outward from the substrate. Since solidification takes a short time owing to its lower molten volume, this resulted in finer columnar grains in A, B, and C, whereas higher heat-input causes higher molten volume, which in turn raises the solidification period with coarser grain size in D, E, and F tracks.

The grain size curve of these six samples of Fig. 3 measured by cross section method against heat-input is shown in Fig. 4. According to the results, increasing the heat-input leads to coarser nuclei, resulting in coarser columnar grains. The figure shows that heating input within the range 425–500 J/mm has the highest impact on the grain size, while the

effect of lower and higher heat-inputs leads to minor changes. In fact, in the case of lower heat-input, the substrate sinks the heating efficiently, while the deposited layers with the highest heat-input approach the saturated condition.

Four-layer walls with various heat-inputs concerning the single layers' results were built to investigate defect-free samples' structure and mechanical properties. The four top heat-input values were used for welding the layers of wall No.1 from the bottom to the top, as shown in Fig. 5. The microstructural analysis reveals that the columnar grains in the top layers are coarser than those in the lower layers. However, despite each layer having lower heat-input than the previous one, the columnar grains in the lower layers have finer columnar grains owing to the substrate heat sink effect. The top layer of the wall shows equiaxed grains, which are coarser than the grains of the previous layer due to the lower cooling rate. As the heat-input increases, the width of the sample increases. This characteristic also shows that increasing heat-input increases penetration depth and width [24].

In Fig. 6, all four layers of wall No.2 were deposited with an average heat-input; the columnar grain size in each layer is increased due to the accumulation of heat in the successive layers [25]. Under the same heat-input conditions, the liquid molten pool spreads more quickly, so the width of the cladding layer increases [26]. Observing a sharp rise in the size of columnar and equiaxed grains in the last layer is a proof of heat accumulation [27].

Wall No.3 was built with the four lowest heat-inputs used in this study, which is shown in Fig. 7. The first layer was deposited with the minimum heat-input of wall No.1, and then the heat-input was reduced layer by layer. Less roughness is observed in the final part, and the wall is closer to the desired final shape due to less total heat-input in the whole process. The general microstructure feature of this wall is similar to wall No.1. However, because of the lower heat-input in the top layer, which balances the effect of a lower cooling rate, finer columnar grains developed comparing with the upper layer in walls No.1 and. 2. Fig. 8 shows the columnar grain sizes for these walls in each layer; due to the lower amount of heat-input, wall 3 has the finest columnar grain sizes of any of the walls. Another observation is that the columnar grain is more enlarged in wall 2 than walls 1 and 3.

Fig. 9 shows the SEM image of the walls' microstructures. The first layer of wall No.1 (Fig. 9d) and wall No.2 (Fig. 9e) has acicular ferrite (AF) and pro-eutectoid ferrite (P-EF) because of the high cooling rate
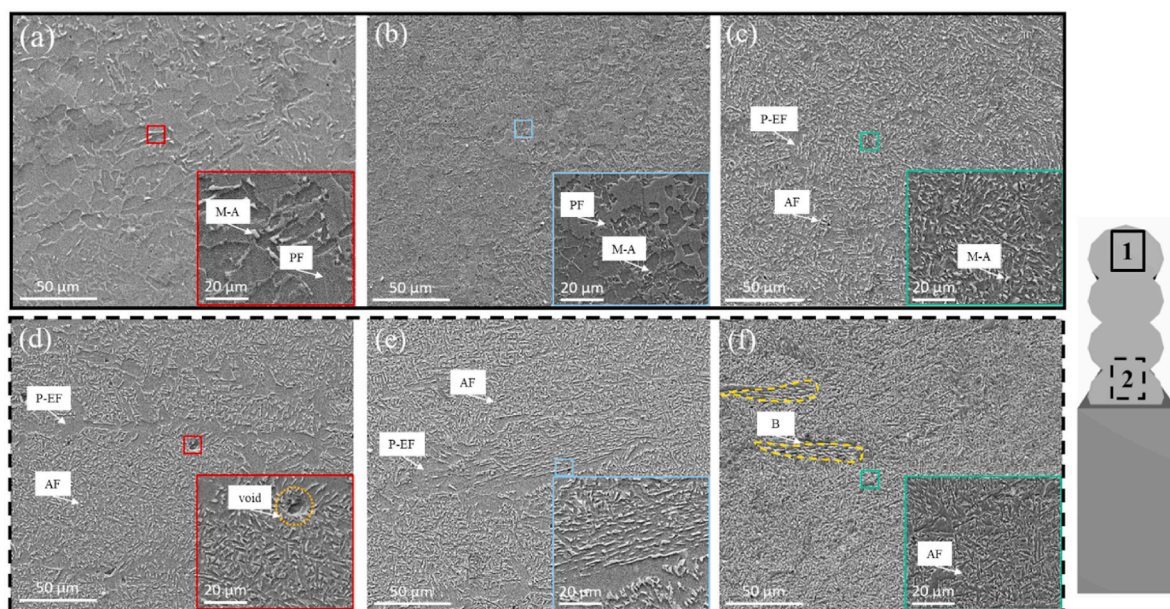

Fig. 9. SEM results from the top layers in the first position from (a) wall 1, (b) wall 2, and (c) wall 3, and the first layers in the second position from (d) wall 1, (e) wall 2, (f) wall 3. (M–A: martensite-austenite, PF: polygonal ferrite, P-EF: pro-eutectoid ferrite, AF: acicular ferrite, B: bainite).
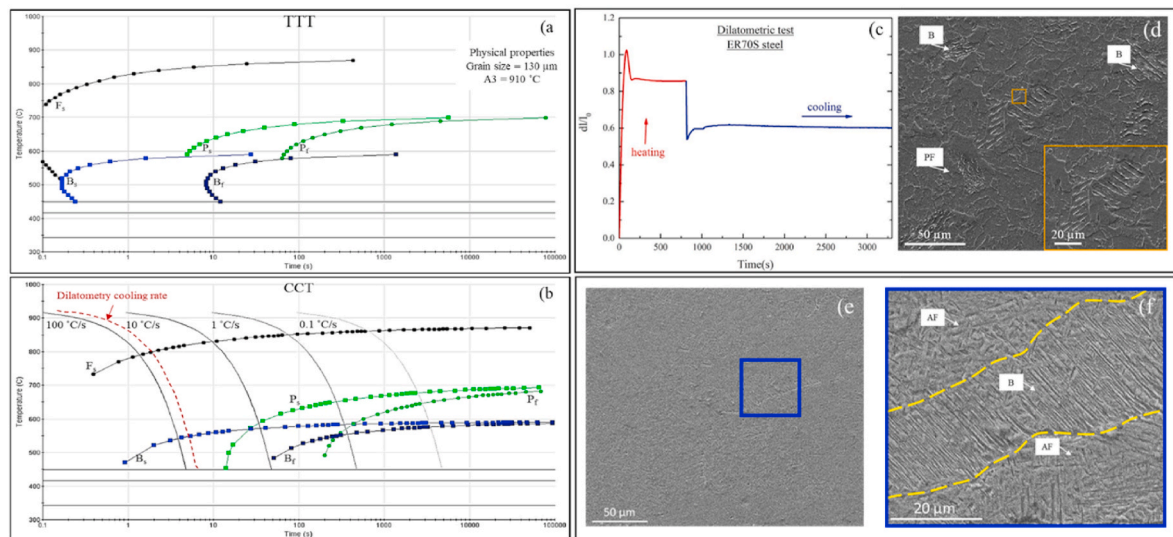
Fig. 10. (a) Time–temperature-transformation (TTT) diagram of the ER70S steel calculated using the JMatPro software, (b) dilatometric curve, and (c) SEM of wall 3 after dilatometric cycle.
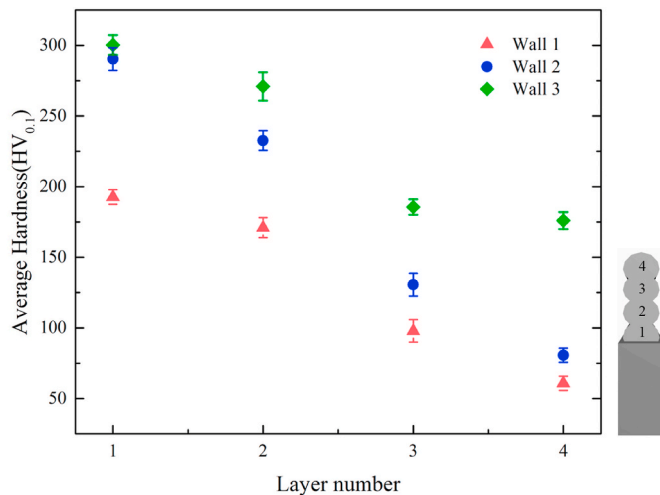

Fig. 11. Vickers hardness profiles of each layer of wall manufactured by the WAAM process.

due to being closer to the substrate. Accelerated cooling promotes the formation of AF because it increases super-cooling and, consequently, the driving force for transformations [28], which raises the nucleation rate and permits AF intergranular nucleation. The high heat-input in the first layer of wall No.1 and the increased cooling rate cause porosity formation during solidification. The cooling from the austenitizing temperature (>800 °C) caused the formation of mostly martensite-austenite (M-A) constituents in the matrix of polygonal ferrite [13]. The top layer of wall No.1 (Fig. 9a) and wall No.2 (Fig. 9b) shows polygonal ferrite (PF) and M-A constituents, but the volume fraction of M-A constituents in wall No.2 is less due to the heat accumulation.

The top layer of wall 3 has a structure of AF, P-EF, and M-A particles due to the lowest heat input and the higher cooling rate than walls 1 and 2. The first layer of this solidifies fast because it is near the substrate, while the second layer re-melts a part of the first layer during deposition but with a lower heat-input than walls 1 and 2, which tolerates the formation of acicular ferrite due to this thermal history. The previous studies on ER70S steel show the formation of bainite in aligned laths shapes [29]. The precipitation of bainite in ER70S steel during WAAM is

mainly controlled by the cooling rate, which should be high enough to prevent entire ferrite formation. The cooling rate is determined by adjusting the welding parameters, such as the heat-input, the travel speed, and the wire feed rate. Higher cooling rates tend to favor bainite formation since it results in a more significant undercooling of the austenite [30]. In plain steels, the appearance and distinction of bainite are somewhat complicated because of the short incubation time of ferrite and the microstructural similarity between AF and bainite. On the other hand, studies show that the structures of acicular ferrite and upper bainite are different in terms of the orientation of the lathes in such a way that parallel lathes with an angle of less than 15° show the structure of upper bainite and chaotic lathes with an angle of more than 15° show acicular ferrite structure [31]. To overcome this ambiguity, the time-temperature-transformation (TTT) diagram of ER70S steel (Fig. 10a) was calculated using the JMatPro software, which only shows the approximate time and temperature of phase transformations. In this calculation, physical properties of the first layer of Wall 3 such as grain size and austenitizing temperature were assumed to be 130 µm and 950 °C (40 °C above A_3), respectively. The output results from the calculated TTT diagram were used for the dilatometry test, and it was performed on the sample from the first layer of wall 3. The figure shows that the bainite transformation start temperature (Bs) is about 590 °C, and the structure of ER70S steel at 500 °C includes bainite in addition to ferrite. Based on the continuous-cooling-transformation (CCT) diagram (Fig. 10b), the sample was heated up to the temperature of 950 °C at a rate of 90 °C/s and successively held for 15 min, then cooled down at a rate of 80 °C/s to 490 °C. During cooling in the dilatometry test, two expansion peaks were observed. The expansion peaks are due to the transformation of austenite to ferrite and the transformation of the retained austenite to bainite (Fig. 10c). The bainite morphology of ER70S steel (Fig. 10d) is similar to the enclosed yellow areas in Fig. 9f, which confirms the microstructure of the first layer of wall 3 is a combination of bainite (B) and AF.

Fig. 10e and f shows another SEM image of the first layer of wall 3 (Fig. 9f). As can be seen, the structure of the first layer of wall 3 includes two morphologies, with parallel lathes and chaotic lathes, which according to the microstructure obtained from the sample after the dilatometry test (Fig. 10d), include acicular ferrite and bainite.

3.2. Microstructure correlation with mechanical properties

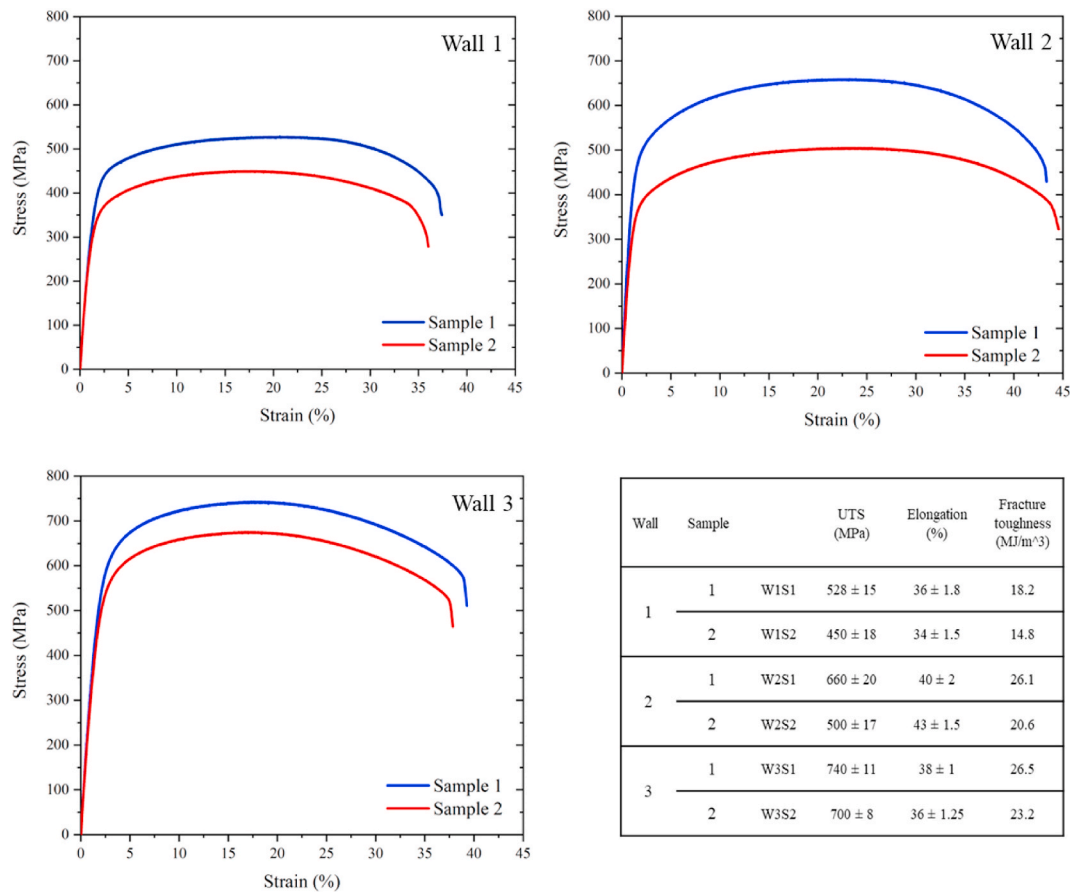It is well understood that the microstructure has a crucial impact on

Fig. 12. The stress-strain curves of sample 1 and sample 2 from each wall manufactured by the WAAM process (*e.g.*, sample code W1S1, refers to wall 1 sample 1).
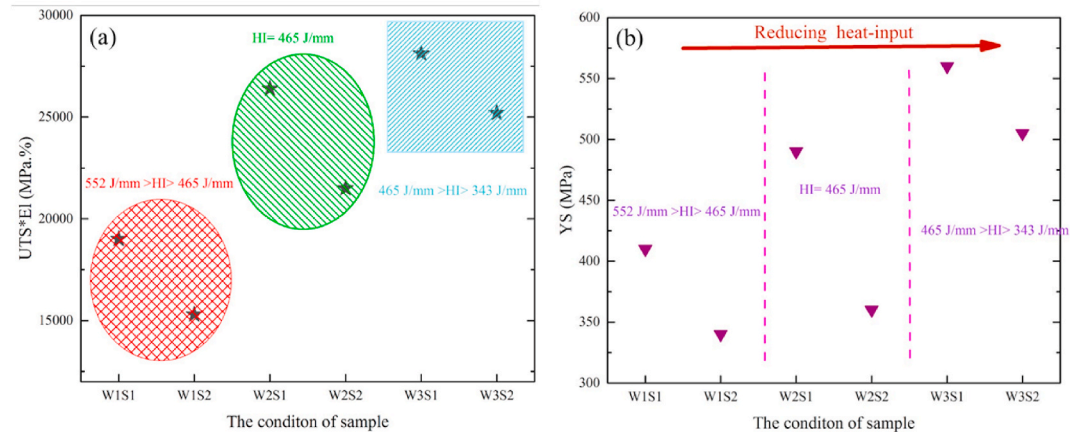
Wall	Sample		UTS (MPa)	Elongation (%)	Fracture toughness (MJ/m^3)
1	1	W1S1	528 ± 15	36 ± 1.8	18.2
	2	W1S2	450 ± 18	34 ± 1.5	14.8
2	1	W2S1	660 ± 20	40 ± 2	26.1
	2	W2S2	500 ± 17	43 ± 1.5	20.6
3	1	W3S1	740 ± 11	38 ± 1	26.5
	2	W3S2	700 ± 8	36 ± 1.25	23.2

Fig. 13. (a) Tensile toughness representative (UTS × Total Elongation) versus the condition of the sample (*e.g.,* W3S1: sample 1 of wall 3), and (b) YS versus the state of the sample.

the mechanical properties of samples manufactured by the WAAM process [32]. In order to assess the effect of heat-input on mechanical properties, a hardness examination of the columnar grains of the walls manufactured by the WAAM process was performed. The results are shown in Fig. 11. The microstructure and, subsequently, the hardness of layers of walls 1 and 3, which were deposited in order of successive heat-input reduction, and wall 2, which had a consistent heat-input, are very different. Wall 1 has the lowest hardness because it faces maximum heat-inputs and has larger columnar grains than the others. The coarseness of columnar grains in the top layers causes a drop in

hardness, but because each layer has received less heat-input, the coarseness of the columnar grains shows a lower slope than wall 2, which in turn, the hardness reduction rate leads to a relatively more downward slope. The same hardness reduction is observed in wall 2 but happens with a higher slope. This is because all the layers are deposited with constant heat-input. The lower cooling rate in the top layers is not compensated, and the coarseness of the columnar grains increases with a higher rate, as revealed by the sharper slope. Due to less heat-input during construction, wall 3 has the highest hardness. The columnar grain size is finer; however, similar to wall 1, the reduction in hardness
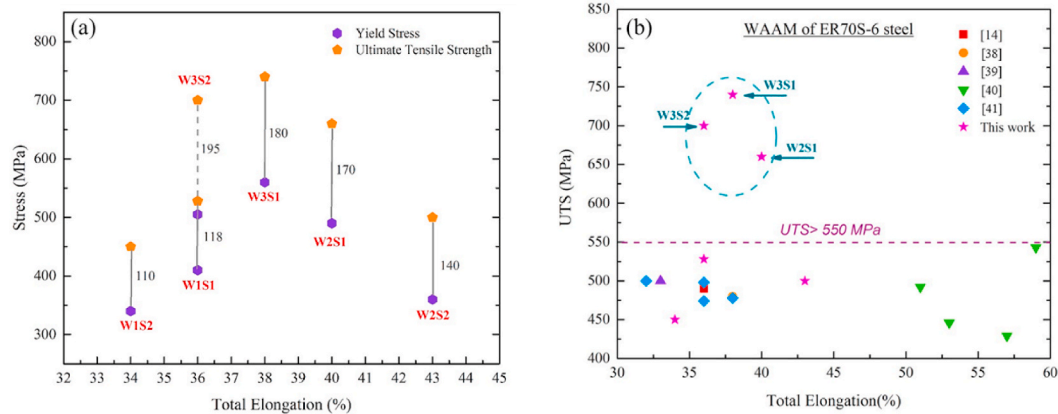
Fig. 14. (a) A summary of tensile properties and absorbing energy during the fracturing versus total elongation, and (b) UTS versus total elongation of ER70S-6 steel manufactured by the GMAW process in present and previous studies.

in the top layers shows a lower slope because less heat was applied to the top layer to compensate for the low cooling rate.

The maximum hardness value observed in the first layer of wall 3 (300 HV) can be attributed to the presence of bainite and acicular ferrite in the microstructure. On the other hand, the minimum hardness observed in the upper layer of wall 1 can be linked to the presence of coarse polygonal ferrite and MA region in the microstructure.

The tensile test of samples 1 and 2 of the walls is shown in Fig. 12. As predicted by the hardness analysis, sample 1 shows a greater ultimate tensile strength (UTS) than sample 2 in all three walls because sample 1 is prepared from layers close to the substrate, where the cooling rate is the highest, leading to finer grains and higher UTS [33]. Wall 1 has the highest elongation among the three walls due to the highest heat-input in all layers and the coarseness of the grains. Wall 3, with a slight decrease in elongation, has the highest UTS value between the three walls due to the lowest heat-input and the formation of finer grains. Wall 2 shows the most non-uniform mechanical properties between sample 1 and sample 2 due to the sudden growth of grains in the layers far from the substrate, which is the effect of heat accommodation [34]. In comparison, the stress-strain curve of these three walls reveals that wall 3 has more uniform properties and finer grains because of lower heat-input and much less heat accumulation in the higher layers due to reduced heat-input in each layer.

Fig. 13 summarizes the mechanical properties of processed walls in this study. Fig. 13a plots the toughness representative (MPa%) versus the samples with the different conditions of the WAAM process. These results implied that the processed wall 3, sample 1 (abbreviated W3S1) presented the maximum value of 28860 MPa%, known as the toughness factor (Ultimate tensile strength × Elongation to failure (UTS × Total Elongation)) or tensile toughness representative [35].

Concerning the dependence of yield strength on average grain size, AM specimens were found to follow the Hall-Petch relationship [36]. The Hall-Petch equation that has been determined through the experiment is used to calculate grain boundary strengthening (σ_{gb}):

$$\sigma_{gb} = K_y d^{-0.5} \tag{2}$$

where d is the grain size, and K_y is the strengthening coefficient. According to the results of Fig. 8, due to lower heat-input in wall 3, in all layers, the grain size is finer. The yield stress and UTS are higher than walls 1 and 2 as predicted by the Hall-Petch relationship (Fig. 13). Therefore, fine grain structure can enhance the deformation compatibility of the whole sample, thereby bringing about a minor reduction in ductility but much higher yield strength, which is shown in Fig. 13b.

The cooling rate significantly affects the microstructure, which in turn influences the material's mechanical properties. Specifically, the highest cooling rate observed in the first layer of wall 3 leads to bainite

and acicular ferrite formation in the microstructure. This results in an increase in UTS but a slight reduction in elongation. Conversely, the minimum cooling rate is observed in the top layer of wall 1, which causes the coarsening of polygonal ferrite and M-A particles, reducing UTS and elongating.

Fig. 14a shows the summary of mechanical properties for all samples. The results show that the difference between UTS and YS in W3S2 is higher than in other models. The values of UTS-YS are one of the indicators that can help with the decision on the work-hardening capacity of the material, which is essential for absorbing energy during the fracturing of the sample [37].

To provide a direct comparison with published data, Fig. 14b summarizes the mechanical properties of ER70S steel processed by WAAM [14,38–41]. According to Fig. 14b, it can be concluded that a superior strength-ductility trade-off along with reasonable tensile toughness has been achieved for W2S1, W3S1, and W3S2 samples compared to other works in this area.

4. Conclusions

As the leading impact of the present research study, the influence of heat-input control strategy on the microstructure and mechanical properties of low-carbon alloy steel (ER70S-6) walls fabricated by the GMAW process was studied. To this end, carbon steel walls were deposited undergoing various processing conditions; the first wall with a reduced heat-input in the range of 552 to 465 J/mm, the second wall with a constant heat-input of 465 J/mm, and the third wall with a decreased heat-input of 496-382 J/mm. Based on the characterization studies and scientific trends, the following conclusions can be drawn:

- The applied heat-input control strategy significantly affected the deposition of layers upon WAAM, their shape, and even the bonding between them. Accordingly, different microstructural features were revealed by the act of this adaptive control of the heating process since less heat-input causes a higher solidification rate resulting in the formation of finer columnar grains.
- The deposited walls show more uniform properties with finer grains due to lower heat accumulation and successively reduced heat-input from the bottom to top layers in wall 3. In contrast, a considerable gradient and heterogeneity across the other manufactured walls were analyzed.
- The microstructure of this wall also shows formations of acicular ferrite and bainite constituents by the controlled heating and cooling cycles upon WAAM processing. As the main result, the contribution of bainite in the microstructure improves the mechanical properties, such as yield strength, tensile strength, and ductility.

- With a more satisfactory strength-ductility trade-off, the mechanical investigations revealed that wall 3 fabricated by WAAM with a hardness of about 300 HV shows a tensile strength of 740 MPa and a remarkable toughness factor of 28.86 GPa%.

Declaration of competing interest

The authors declare that they have no known competing financial interests or personal relationships that could have appeared to influence the work reported in this paper.

Acknowledgement

References

[1] Vaz RF, Silvello A, Albaladejo V, Sanchez J, Cano IG. Improving the wear and corrosion resistance of maraging part obtained by cold gas spray additive manufacturing. Metals 2021;11(7):1092.

[2] Ghafoori E, et al. Fatigue strengthening of damaged steel members using wire arc additive manufacturing. Eng Struct 2023;284:115911.

[3] DebRoy T, Wei HL, Zuback JS, Mukherjee T, Elmer JW, Jo Milewski, Beese AM, Wilson-Heid A, De A, Zhang W. Additive manufacturing of metallic components–Process, structure and properties. Prog Mater Sci 2018;92:112–224.

[4] Li JZ, Alkahari MR, Rosli NAB, Hasan R, Sudin MN, Ramli FR. Review of wire arc additive manufacturing for 3D metal printing. Int J Autom Technol 2019;13(3): 346–53.

[5] Gudeljevic M, Klein T. Investigation of material characteristics of intersections built by wire and arc additive manufacturing using locally varying deposition parameters. Int J Adv Des Manuf Technol 2021;116(5).

[6] Ugla A, Khaudair HJ, Almusawi AR. Metal inert gas welding-based-shaped metal deposition in additive layered manufacturing: a review. World Academy of Science, Engineering and Technology International Journal of Mechanical and Materials Engineering 2019;13(3).

[7] Cunningham C, Flynn J, Shokrani A, Dhokia V, Newman S. Invited review article: strategies and processes for high quality wire arc additive manufacturing. Addit Manuf 2018;22:672–86.

[8] Herzog D, Seyda V, Wycisk E, Emmelmann C. Additive manufacturing of metals. Acta Mater 2016;117:371–92.

[9] Xu X, Ganguly S, Ding J, Guo S, Williams S, Martina F. Microstructural evolution and mechanical properties of maraging steel produced by wire+ arc additive manufacture process. Mater Char 2018;143:152–62.

[10] Wang T, Zhang Y, Wu Z, Shi C. Microstructure and properties of die steel fabricated by WAAM using H13 wire. Vacuum 2018;149:185–9.

[11] de Albuquerque Vicente A, D'silva PA, Babu R, Santos A. The correct choice among welding wires ER70S-2, ER70S-3 and ER70S-6, according to the oxidation level of base metal. Int J Adv Eng Research and Sci 2020;7(8):131–9.

[12] Bellamkonda PN, Sudersanan M, Visvalingam B. Mechanical properties of wire arc additive manufactured carbon steel cylindrical component made by cold metal transferred arc welding process. Mater Test 2022;64(2):260–71.

[13] Nemani AV, Ghaffari M, Nasiri A. Comparison of microstructural characteristics and mechanical properties of shipbuilding steel plates fabricated by conventional rolling versus wire arc additive manufacturing. Addit Manuf 2020;32:101086.

[14] Vahedi Nemani A, Ghaffari M, Nasiri A. On the post-printing heat treatment of a wire arc additively manufactured ER70S part. Materials 2020;13(12):2795.

[15] Kok Y, et al. Anisotropy and heterogeneity of microstructure and mechanical properties in metal additive manufacturing: a critical review. Mater Des 2018;139: 565–86.

[16] Yadollahi A, Shamsaei N, Thompson SM, Seely DW. Effects of process time interval and heat treatment on the mechanical and microstructural properties of direct laser deposited 316L stainless steel. Mater Sci Eng, A 2015;644:171–83.

[17] Greebmalai J, Warinsiriruk E. Multi-heat input technique for aluminum WAAM using DP-GMAW process. In: AIP conference proceedings. vol. 2279. AIP Publishing LLC; 2020, 050001. 1.

[18] Cui J, Yuan L, Commins P, He F, Wang J, Pan Z. WAAM process for metal block structure parts based on mixed heat input. Int J Adv Des Manuf Technol 2021;113: 503–21.

[19] Derakhshandeh A, Shahmir H, Nili-Ahmadabadi M. Microstructure and mechanical properties of ultrafine-grained titanium processed by multi-pass ECAP at room temperature using core–sheath method. J Mater Res 2018;33(22):3809–17.

[20] Kumar K, et al. Optimisation of thickness of miniature tensile specimens for evaluation of mechanical properties. Mater Sci Eng, A 2016;675:32–43.

[21] Fereiduni E, Ghasemi A, Elbestawi M. Characterization of composite powder feedstock from powder bed fusion additive manufacturing perspective. Materials 2019;12(22):3673.

[22] Yilmaz O, Ugla AA. Microstructure characterization of SS308LSi components manufactured by GTAW-based additive manufacturing: shaped metal deposition using pulsed current arc. Int J Adv Des Manuf Technol 2017;89(1):13–25.

[23] Ding H, Shen N, Shin YC. Modeling of grain refinement in aluminum and copper subjected to cutting. Comput Mater Sci 2011;50(10):3016–25.

[24] González J, Rodríguez I, Prado-Cerqueira J, Diéguez J, Pereira A. Additive manufacturing with GMAW welding and CMT technology. Procedia Manuf 2017; 13:840–7.

[25] Park J, Lee SH. CMT-based wire Arc Additive manufacturing using 316L stainless steel (2): solidification map of the multilayer deposit. Metals 2021;11(11):1725.

[26] Chen C, Sun G, Du W, Liu J, Zhang H. Effect of equivalent heat input on WAAM Al-Si alloy. Int J Mech Sci 2023;238:107831.

[27] Lee SH. CMT-based wire arc additive manufacturing using 316L stainless steel: effect of heat accumulation on the multi-layer deposits. Metals 2020;10(2):278.

[28] Loder D, Michelic SK, Bernhard C. Acicular ferrite formation and its influencing factors—a review. J Mater Sci Res 2017;6(1):24–43.

[29] Francis R, Jones J, Olson D. Effect of shielding gas oxygen activity on weld metal microstructure of GMA welded microalloyed HSLA steel. Weld J 1990;69(11):408.

[30] Olasolo M, Uranga P, Rodriguez-Ibabe J, López B. Effect of austenite microstructure and cooling rate on transformation characteristics in a low carbon Nb–V microalloyed steel. Mater Sci Eng, A 2011;528(6):2559–69.

[31] Costin WL, Lavigne O, Kotousov A. A study on the relationship between microstructure and mechanical properties of acicular ferrite and upper bainite. Mater Sci Eng, A 2016;663:193–203.

[32] Gordon JV, Vinci RP, Hochhalter JD, Rollett AD, Harlow DG. Quantification of location-dependence in a large-scale additively manufactured build through experiments and micromechanical modeling. Materialia 2019;7:100397.

[33] Ermakova A, Mehmanparast A, Ganguly S, Razavi J, Berto F. Investigation of mechanical and fracture properties of wire and arc additively manufactured low carbon steel components. Theor Appl Fract Mech 2020;109:102685.

[34] Dirisu P, Ganguly S, Mehmanparast A, Martina F, Williams S. Analysis of fracture toughness properties of wire+ arc additive manufactured high strength low alloy structural steel components. Mater Sci Eng, A 2019;765:138285.

[35] Heydarinia A, Mohri M, Asghari-Rad P, Kim HS, Nili-ahmadabadi M. Free volume formation and the high strength of pure Mg after room temperature core-sheath ECAP passes. J Mater Res Technol 2022;18:147–58.

[36] Xu W, et al. Additive manufacturing of strong and ductile Ti–6Al–4V by selective laser melting via in situ martensite decomposition. Acta Mater 2015;85:74–84.

[37] Sohrabi M, Mirzadeh H, Mehranpour M, Heydarinia A, Razi R. Aging kinetics and mechanical properties of copper-bearing low-carbon HSLA-100 microalloyed steel. Arch Civ Mech Eng 2019;19(4):1409–18.

[38] Ron T, Levy GK, Dolev O, Leon A, Shirizly A, Aghion E. Environmental behavior of low carbon steel produced by a wire arc additive manufacturing process. Metals 2019;9(8):888.

[39] Rafieazad M, Ghaffari M, Vahedi Nemani A, Nasiri A. Microstructural evolution and mechanical properties of a low-carbon low-alloy steel produced by wire arc additive manufacturing. Int J Adv Des Manuf Technol 2019;105:2121–34.

[40] Nagasai BP, Malarvizhi S, Balasubramanian V. Effect of welding processes on mechanical and metallurgical characteristics of carbon steel cylindrical components made by wire arc additive manufacturing (WAAM) technique. CIRP J Manufacturing Sci Technol 2022;36:100–16.

[41] Aldalur E, Veiga F, Suárez A, Bilbao J, Lamikiz A. High deposition wire arc additive manufacturing of mild steel: strategies and heat input effect on microstructure and mechanical properties. J Manuf Process 2020;58:615–26.